TROPICAL CYCLONE RESEARCH REPORT
TCRR **1**: 1–15 (2019)
Meteorological Institute
Ludwig Maximilians University of Munich

Contribution of mean and eddy momentum processes to tropical cyclone intensification

M. T. Montgomery[a], Gerard Kilroy[b], Roger K. Smith[b] and Nina Črnivec[b]

[a] *Dept. of Meteorology, Naval Postgraduate School, Monterey, CA*
[b] *Meteorological Institute, Ludwig-Maximilians University of Munich, Munich, Germany*

Abstract:
A high-resolution, three-dimensional, numerical simulation of a rapidly-intensifying tropical cyclone is used to extend basic knowledge on the role of mean and eddy momentum transfer on the dynamics of the intensification process. Examination of terms in *both* the tangential and radial velocity tendency equations provides an improved quantitative understanding of the dynamics of the spin up process within the inner-core boundary layer and eyewall regions of the system-scale vortex. Unbalanced and non-axisymmetric processes are prominent features of the rapid spin up process. In particular, the wind asymmetries, associated in part with the asymmetric deep convection, make a substantive contribution (∼30%) to the maximum wind speed inside the radius of this maximum. The analysis provides a novel explanation for inflow jets sandwiching the upper tropospheric outflow layer that are frequently found in numerical model simulations. In addition, it provides an opportunity to assess the applicability of generalized Ekman balance during vortex spin up. The maximum tangential wind occurs within and near the top of the frictional inflow layer and as much as 10 km inside the maximum gradient wind. Spin up in the friction layer is accompanied by supergradient winds that exceed the gradient wind by up to 20%. Overall, the results affirm prior work pointing to significant limitations of a purely axisymmetric balance description, e.g., gradient balance/Ekman balance, when applied to a rapidly-intensifying tropical cyclone.

KEY WORDS Hurricane; tropical cyclone; typhoon; boundary layer; vortex intensification

Date: January 20, 2020; Revised ; Accepted

1 Introduction

The problem of understanding tropical cyclone intensity change has been at the cutting edge of meteorological research in recent years, especially in the context of the rapid intensification or rapid decay of storms threatening landfall in populated coastal communities. This is because of the continued challenges in forecasting intensity change, a phenomenon which involves processes with scales spanning many orders of magnitude.

Most of the available paradigms for understanding tropical cyclone intensification are based, for simplicity, on axisymmetric models and most have considered the prototype problem, which addresses the evolution of an initially cloud-free, warm-cored, symmetric vortex in gradient wind and hydrostatic balance in a quiescent environment on an f-plane. However, such models have been shown to have inherent limitations for understanding the intensification process because they represent convection in the form of axisymmetric rings (Persing *et al.* 2013).

As shown in many previous studies, for much of the intensification phase of a simulated storm, the flow is markedly asymmetric (Montgomery *et al.* 2006; Nguyen *et al.* 2008; Fang and Zhang 2011; Persing *et al.* 2013; Kilroy *et al.* 2016; Raymond and Kilroy 2019). This is because deep convective structures, which are a key component of the intensification process, are intrinsically three dimensional and their locations within the vortex have a stochastic element. In fact, the azimuthally-averaged fields of, for example, vertical velocity, vertical vorticity, diabatic heating rate and regions of saturation are *dominated* by such structures. Accordingly, eddy processes and the accompanying asymmetric vortex waves must be an integral part of a complete dynamical explanation of the vortex behaviour.

For the foregoing reasons, a paradigm for tropical cyclone intensification that incorporates the three-dimensional nature of deep convection has been developed over the last decade or more, the so-called *rotating-convection paradigm*. The rotating-convection paradigm is reviewed by Smith and Montgomery (2016) and Montgomery and Smith (2014, 2017) in the context of the prototype problem. While the main focus of the rotating-convection paradigm has been on the dynamical mechanisms involved in the spin up process, the paradigm acknowledges the need for a modest elevation of surface enthalpy fluxes to sustain the deep convection required for vortex spin up. On the dynamical side, it has been recognized for some time that the intensification of a realistic tropical cyclone involves marked deviations from classical axisymmetric balance dynamics, which assumes a

[1]Correspondence to: Prof. M. T. Montgomery, Department of Meteorology, Naval Postgraduate School, Monterey, CA USA. E-mail: mtmontgo@nps.edu

slow evolution of an axisymmetric vortex in strict gradient and hydrostatic balance subject to forcing by heat release and tangential momentum sources or sinks. Such deviations were highlighted by a high resolution (at that time, $\delta x = 6$ km) simulation of Hurricane Andrew (1992) by Zhang *et al.* (2001). These authors set out, *inter alia*, to answer three main questions: "To what extent is the gradient wind balance model a good approximation to the local and azimuthally averaged tangential winds in an intensifying hurricane? What causes the gradient wind imbalance locally and in an azimuthally averaged state? What is the intensifying mechanism of tangential winds in the eyewall?"

Their answer to the first question was yes, to a degree within approximately 10%. However, supergradient winds were found to be an important feature of the corner flow region of the simulated storm and also in the eyewall where the air motion has an outward component. Zhang *et al.* (p106) explained the development of the supergradient wind and spin up of the eyewall as follows: "As the storm deepens, the cross-isobaric radial inflow in the marine boundary layer transports more absolute angular momentum from the hurricane environment into the eyewall region than frictional dissipation. The major radial inflow decelerates as it approaches the radius of maximum wind where the centrifugal force exceeds radial pressure gradient force. ... Then, all the inflow air mass must ascend in the eyewall, transporting absolute angular momentum upward to spin up the tangential flow above. This upward transport of absolute angular momentum could increase significantly the local centrifugal force, thereby causing the pronounced supergradient acceleration and the development of radial outflow in the eyewall. In the present case, the supergradient acceleration occurs at the same order of magnitude as radial pressure gradient force in the vicinity of V_{max} (the maximum wind speed, our insertion), and accounts for the generation of an outflow jet near the top of the marine boundary layer. However, the local changes in tangential winds are always small due to the intense advection in the eyewall. It is evident that (a) the intensity of the radial outflow depends critically on the upward transport of absolute angular momentum, and (b) the spindown of the eyewall by radial outflow must be overcompensated by the upward transport of absolute angular momentum if the storm is to deepen. Of course, the underlying ocean (and latent heat release in the eyewall) is the fundamental energy source for the deepening of tropical cyclones."

According to the above view, the evaporation of water from the underlying ocean supports a nonlinear spin up process wherein the development of supergradient winds in the boundary layer of the vortex, in combination with the upward transport of absolute angular momentum from the boundary layer, play an important role in the intensification of the storm's eyewall cloud. Similar findings were reported in idealized, but finer resolution numerical simulations by Smith *et al.* (2009) and Persing *et al.* (2013). In particular, Persing *et al.* showed that the spinup of the eyewall in the lower troposphere was accomplished primarily by resolved vertical eddy momentum fluxes in their three-dimensional configuration (Persing *et al.* 2013, cf. Figs. 10d,g,h). The nonlinear dynamics of the vortex boundary layer and its contribution in spinning up the eyewall was discussed further from the perspective of the newly developed rotating-convection paradigm by Montgomery and Smith (2017). The upshot of the foregoing findings is that if unbalanced and eddy processes play a marked role in spinning up a tropical cyclone eyewall, a more complete understanding of the dynamics of the tropical cyclone boundary layer and interior is certainly warranted.

In the present study we investigate further the salient dynamical attributes in both the boundary layer and vortex interior that support the rapid intensification of the vortex. We examine also hitherto unexplored features of the flow in the upper troposphere. In particular, we aim to (i) quantify the relative contributions of the mean and eddy covariance terms to the tangential and radial accelerations in the vortex core region (including the departure from gradient wind balance), extending the work of Persing *et al.* (2013) and Zhang *et al.* (2001); (ii) assess the validity of generalized Ekman balance (Smith and Montgomery 2019) in the inner-core boundary layer during rapid intensification; and, (iii) to investigate and offer an explanation for inflow jets sandwiching the upper tropospheric outflow layer, structures which are frequently found in numerical model simulations (for example: Figs. 15a, 17a of Persing *et al.* (2013); Fig. 2 of Ohno and Satoh (2015), Fig. 2 of Kilroy *et al.* 2018; Fig 2b,d of Smith *et al.* 2018). As far as we are aware, there has been no satisfactory explanation for these upper-level inflow jets.

The remaining paper is organized as follows. The numerical model used and an overview of the numerical simulation are presented in section 2. Section 3 summarizes certain aspects of the simulated vortex evolution, including a quantitative assessment of the wind asymmetries in relation to the maximum wind speed in the boundary layer. Section 4 quantifies and interprets the role of mean and eddy processes mentioned above on the azimuthal-mean tangential and radial wind tendencies during vortex spin up. This analysis includes an examination of the development of upper-tropospheric inflow jets and generalized Ekman balance. A summary and conclusions are presented in section 5.

2 The numerical model

The numerical model used for the study is version 16 of the three-dimensional, nondydrostatic cloud model CM1, (Bryan and Fritsch, 2002). In brief, the model has prediction equations for the three components of the velocity vector, specific humidity, suspended liquid, perturbation Exner function, and perturbation density potential temperature, where perturbation quantities are defined relative to a prescribed hydrostatic basic state. For simplicity, the Kessler warm rain scheme is used in which rain has a fixed fall speed of 7 m s^{-1}. For simplicity, ice microphysical processes and dissipative heating are not included. The calculations here are carried out for a period of 5 days with data output every 15 min.

A latitude of 20^{o}N and a constant sea surface temperature of 27^{o}C are assumed. The model configuration is similar to that described in section 2 of Črnivec *et al.* (2016), except that a potentially more realistic time scale for Newtonian relaxation to the temperature field (10 days) is applied here instead of the previous default CM1 value (12 hours): see Mapes and Zuidema (1996). [1]

The model domain is 3010 $\times$ 3010 km, with 1040 grid points in the x and y directions. The inner 600 $\times$ 600 km of the domain has a constant horizontal grid spacing of 1 km, while in the outer domain, the grid spacing is stretced gradually from 1 km to 10 km. There are 68 vertical levels starting at a height of 50 m and extending upwards to a height of 25 km. The vertical grid spacing is 50 m in the lowest 1 km, above which it stretches smoothly to 1200 m near the model top.

To suppress the artificial reflection of internal gravity waves from the upper boundary, a Rayleigh damping layer is added at heights above 20 km. The lateral boundaries are open radiative.

The background thermodynamic state is based on the Dunion moist tropical sounding (Dunion, 2011). This sounding has a Convective Available Potential Energy of 2104 J kg^{-1} and a Total Precipitable Water of 51.5 kg m^{-2}.

The values for the sub grid-scale turbulence mixing lengths are based on the recent observational findings of Zhang and Montgomery (2012) and Zhang *et al.* (2011), respectively, and the resulting vertical and horizontal eddy diffusivities output in prior model simulations of Persing *et al.* (2013). The chosen values of horizontal mixing length $l_h = 700$ m and vertical mixing length $l_v = 50$ m are close to the values recommended by Bryan (2012) in order to produce realistic hurricane structure. For simplicity, these mixing lengths are assumed constant in both space and time.

The initial vortex is axisymmetric and in thermal wind balance. The initial tangential wind speed has a maximum of 15 m s^{-1} at the surface and at a radius of 100 km. The tangential wind speed decreases sinusoidally with height, becoming zero at a height of 20 km. Above this height, the tangential wind is set to zero.

The balanced pressure, density and temperature fields consistent with this prescribed tangential wind distribution are obtained using the method described by Smith (2006). The choice of this relatively strong initial vortex bypasses the genesis phase, which was examined in detail, for example, by Kilroy *et al.* (2017) and refs.

[1]With a 10 d relaxation time scale, there is some warming of the far field environment, especially at upper levels, after about 4-5 days of integration. This warming does not occur with the default, smaller, time scale. We have found in our previous studies of real life events in the European Centre for Medium Range Weather Forecasts operational analyses (not shown) that the large-scale environment surrounding tropical cyclones warms on the order of about 2-4 K over a ten day period (as seen, for example, in averaged temperature difference plots of Tropical cyclone George (2007) and Tropical cyclone Carlos (2011)). These findings provide some evidence that the default time scale for relaxation in CM1 is strongly over-relaxing to the initial sounding in the case of a mature hurricane. In any case, with a 10 d relaxation time scale, there is not sufficient warming on the order of 5 d to strongly affect vortex evolution. In the simulation presented here the far field warms by about 1 K between heights of 5 and 15 km over the 5 d time period integrated.

3 Some aspects of vortex evolution

To provide a context for the analysis of mean and eddy effects we summarize briefly the time evolution of the vortex and then present characteristics of the low-level flow field during the spin up phase. In the diagnostic analyses presented here we use a cylindrical polar coordinate system (r, λ, z), where r is the radius, λ is the azimuth and z is the height, and corresponding velocity components (u, v, w). The axis of coordinates is located at the surface pressure minimum[2].

3.1 Time series of v_{max}

Figure 1 shows a time series of the maximum azimuthally-averaged tangential wind speed (v_{max}) and maximum total wind speed (vT_{max}) during the 5-day integration period. Following a brief gestation period lasting about 24 h, the vortex begins a period of rapid intensification (RI), lasting from about 24 to 96 h. At this time the vortex reaches its mature stage, with a maximum intensity of about 81 m s^{-1}. The vertical lines shown in the figure highlight times for which extensive analyses will be presented later.

Significantly, vT_{max} exceeds v_{max} as soon as deep convection forms early in the gestation period. The difference between these two quantities, which is typically up to 10 m s^{-1}, quantifies the distinction between mean tangential velocity and total wind speed, the latter of which includes the azimuthally-averaged tangential velocity and radial inflow and wind eddies also. The heights of both v_{max} and vT_{max} are typically below 1 km, within the frictional boundary layer.

3.2 Low-level radial wind profiles

We examine next the low-level wind structure in the high wind speed region of the developing vortex at selected times. This analysis will prove useful later in our interpretation of the horizontal momentum dynamics of the inner-core vortex.

[2]The vortex centre location is obtained by finding the minimum in a filtered surface pressure field, subject to the requirement that the vortex does not move more than 20 km in a single output time. This requirement prevents the centre-finding algorithm from locking on to a localized region of strong convection. Since there is no ambient vertical shear in the problem, it is reasonable to take the centre location to be independent of height.

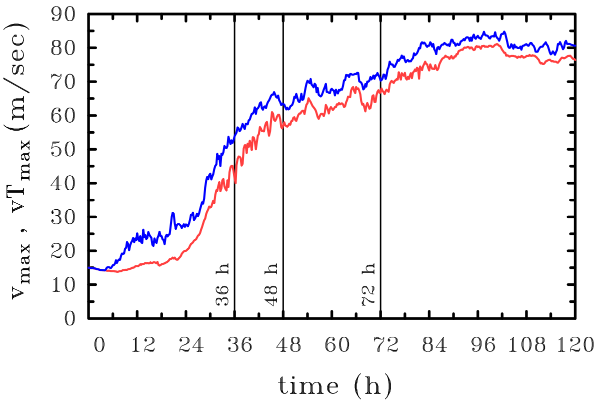

Figure 1. Time series of (a) maximum azimuthally-averaged tangential wind speed (v_{max}, red curve) and maximum total wind speed (vT_{max}, blue curve). The different phases of evolution discussed in the text are identified by thin vertical lines.

Figure 2 shows radial profiles of the azimuthally-averaged tangential velocity component, v, the corresponding gradient wind[3], v_{gr}, at roughly the height of the tangential wind maximum (725 m), and the similarly averaged radial velocity component, u, at the lowest model level (25 m) at 48 h and 72 h during the RI phase. Shown also are the radial profiles of maximum total wind speed $vT = \max\sqrt{u^2+v^2}$ and maximum total eddy wind speed vTp in the lowest 1 km at each radius. The total eddy wind speed is defined as $\max(\sqrt{u'^2+v'^2})$, where a prime denotes the difference between the total and azimuthally-averaged variable.

At 36 h, v is approximately equal to v_{gr} beyond a radius of 45 km, but there are small amplitude fluctuations of the difference. The maximum tangential wind is 41.3 m s^{-1} and occurs at a radius, r_{vmax}, of 34 km, while the maximum gradient wind is 38.3 m s^{-1} and occurs at a radius of 33 km. Between radii of 15 km and 45 km, v exceeds v_{gr}, i.e. the tangential wind is supergradient. At r_{vmax}, v exceeds v_{gr} by 9.2%, while vT exceeds v at all radii and has its maximum at a radius outside r_{vmax}. The near surface radial wind has a maximum of 15.9 m s^{-1} at a radius of 41 km, the maximum being 38% of v_{max}. Notably, vTp retains a high degree of variability out to 100 km radius, suggesting that the total eddy wind speed remains a significant component of the total flow throughout the inner core region.

At 48 h and 72 h, the results are broadly similar to the findings at 36 h, but the velocity maxima contract inwards with time and amplify considerably. For example, at 48 h, v_{max} is 56.5 m s^{-1} while the maximum gradient wind is only 47 m s^{-1} and the near surface maximum inflow is 22 m s^{-1}. At this time, r_{vmax} is 26 km, while the radius of the maximum gradient wind is 34 km. Further, at r_{vmax}, the tangential wind is supergradient by 22%. The total wind speed vT exceeds the tangential wind v at all radii and again, at this time, has its maximum at a radius inside r_{vmax}

At 72 h, v_{max} is 66.5 m s^{-1} while the maximum gradient wind is only 52 m s^{-1} and the near surface maximum inflow is 27.5 m s^{-1}. At this time, r_{vmax} is 31 km (slightly outside that at 48 h), while the radius of the maximum gradient wind is 37 km. Further, at r_{vmax}, the tangential wind is supergradient by 27.8%. Once again, vT exceeds v at all radii and, at this time, has its maximum at a radius inside r_{vmax}. As at 36 h and 48 h, the difference between vT and v and the eddy wind speed vTp profile reflect the presence of wind speed asymmetries. The total eddy wind speed remains a significant component of the total flow inside r_{vmax}. Presumably, the confinement of the maximum wind asymmetries to the region inside r_{vmax} is a reflection of the focussing of deep convection to the eyewall region of the mature vortex.

Overall, the results indicate that *the radial component of near-surface flow is a significant fraction of the tangential wind speed* and affirm the findings of Zhang *et al.* (2001) that *gradient-wind imbalance is an intrinsic feature of the boundary layer dynamics* during vortex spin up.

4 Analysis of mean and eddy processes during vortex intensification

During intensification, multiple vortical updraughts have been shown to be a ubiquitous feature of the inner-core circulation. These updraughts act collectively to draw air parcels inwards in the low- to mid-troposphere, above the vortex boundary layer, and concentrate cyclonic vorticity in this layer. These updraughts have been shown to contribute to the sign and structure of the eddy momentum fluxes in the azimuthally-averaged tangential acceleration equation (Persing *et al.* 2013). The updraughts have been shown also to excite vortex Rossby and inertia-buoyancy waves (e.g., Chen *et al.* 2003, Reasor & Montgomery 2015), that in turn contribute to the eddy momentum fluxes and divergence in the tangential acceleration equation. Thus, during spin up, a complex turbulent system of rotating, deep moist convection and vortex waves comprises the eddy field of the cloudy vortex core.

A more complete understanding of the complex eddy dynamics is certainly warranted and here we take a next step in quantifying the net signatures of the updraughts and related vortex waves in the eddy terms and corresponding mean terms in the horizontal momentum equations during vortex spin up. In particular, we extend the Persing *et al.* analysis who examined, *inter alia*, the mean and eddy contributions to the azimuthal-mean tangential wind tendency equation. Here we employ a higher horizontal resolution (1 km grid spacing in the inner-vortex region) and examine also the eddy and mean contributions to the corresponding radial velocity tendency equation during spin up. The latter analysis enables one to quantify in a

[3]The gradient wind, v_g, is obtained by solving the quadratic equation $\frac{v_g^2}{r} + fv_g - \frac{1}{\rho}\frac{\partial p}{\partial r} = 0$.

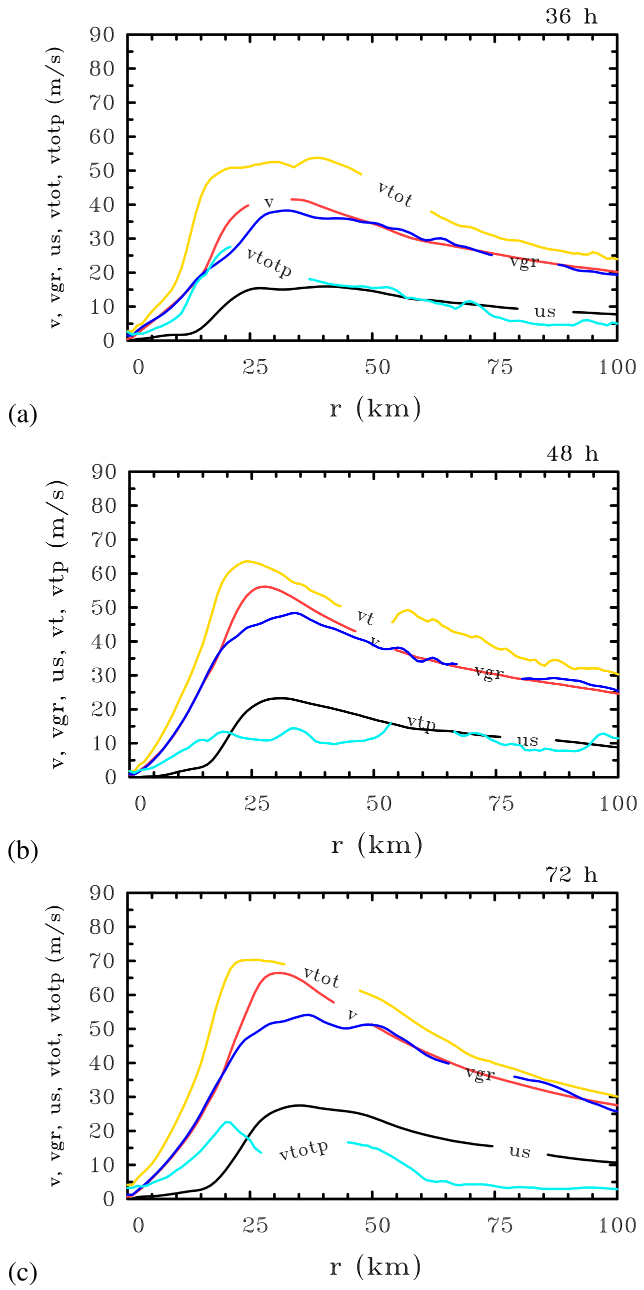

Figure 2. Radial profiles of azimuthally-averaged tangential wind (labeled 'v') and gradient wind (labelled 'vgr') at a height of 725 m at (a) 36 h, (b) 48 h and (c) 72 h. Shown also are radial profiles of azimuthally-averaged radial *inflow* (labeled 'us' where 's' refers to the surface) at the lowest model level (25 m), the maximum total wind speed (labeled 'vtot') and maximum total eddy wind speed (labeled 'vtotp' where 'p' refers to perturbation). The last two quantities are not spatially averaged and can occur anywhere in the lowest 1 km.

dynamically-consistent framework: (a) the degree of gradient wind imbalance in relation to other terms in the radial acceleration equation; (b) the role of unbalanced flow processes in the spin up of the inner-core boundary layer, the eyewall updraught complex and upper-tropospheric inflow layers; and, (c) the departure from generalized Ekman balance (Smith and Montgomery 2019).

4.1 Azimuthal mean tendency equations for horizontal velocity

In a cylindrical polar coordinate system defined relative to an approximate invariant center of circulation, the tangential and radial momentum equations may be written, respectively, as

$$\frac{\partial v}{\partial t} + u\frac{\partial v}{\partial r} + \frac{v}{r}\frac{\partial v}{\partial \lambda} + w\frac{\partial v}{\partial z} + (f + \frac{v}{r})u = -\frac{1}{\rho r}\frac{\partial p}{\partial \lambda} + F_\lambda, \tag{1}$$

and

$$\frac{\partial u}{\partial t} + u\frac{\partial u}{\partial r} + \frac{v}{r}\frac{\partial u}{\partial \lambda} + w\frac{\partial u}{\partial z} - \frac{v^2}{r} - fv = -\frac{1}{\rho}\frac{\partial p}{\partial r} + F_r, \tag{2}$$

where (u, v, w) is the three-dimensional velocity vector (u radial, v tangential and w vertical velocities), t is the time, f is the Coriolis parameter, ζ is the vertical component of relative vorticity, F_r and F_λ are the radial and tangential components of the subgrid-scale eddy-momentum flux divergence, and ρ is the density. We define an azimuthal averaging operator by the equation

$$\bar{\gamma} = \frac{1}{2\pi r}\int_o^{2\pi} \gamma r d\lambda, \tag{3}$$

and set any dependent variable γ as the sum of a mean part $\bar{\gamma}$, and an asymmetry (or eddy) γ', i.e. $\gamma = \bar{\gamma} + \gamma'$. Then, noting that, by definition, $\overline{\gamma'} = 0$, we obtain, for example, the azimuthally-averaged tangential form of the velocity tendency equation:

$$\frac{\partial \bar{v}}{\partial t} = \underbrace{-\bar{u}(\bar{\zeta} + f)}_{V_{m\zeta}} \underbrace{-\bar{w}\frac{\partial \bar{v}}{\partial z}}_{V_{mv}} \underbrace{-\overline{u'\zeta'}}_{V_{e\zeta}} \underbrace{-\overline{w'\frac{\partial v'}{\partial z}}}_{V_{ev}} + \underbrace{\bar{F_\lambda}}_{V_d}. \tag{4}$$

Here, we have neglected the azimuthally-averaged pressure gradient term involving perturbations of density in the azimuthal direction. As noted by Persing *et al.* (2013), this term (V_{ppg} in their Equation (12)) is tiny compared with all other terms. The five terms on the right hand size of the Equation (4) are, in order: $V_{m\zeta}$ is the mean radial influx of absolute vertical vorticity, V_{mv} is the mean vertical advection of mean tangential momentum, $V_{e\zeta}$ is the eddy radial vorticity flux, V_{ev} is the vertical advection of eddy tangential momentum, and V_d is the combined mean horizontal and vertical diffusive tendency of tangential momentum, given by:

$$\bar{F_\lambda} = \underbrace{\frac{1}{r^2\bar{\rho}}\frac{\partial r^2 \bar{\rho}\,\overline{\tau_{r\lambda}}}{\partial r}}_{V_{dr}} + \underbrace{\frac{1}{\bar{\rho}}\frac{\partial \bar{\rho}\,\overline{\tau_{\lambda z}}}{\partial z}}_{V_{dz}}, \tag{5}$$

where the stress tensors (e.g., Landau and Lifshitz (1966, p51) - generalized to account for anisotropic eddy momentum diffusivities) for the subgrid scale motions are given by

$$\overline{\tau_{r\lambda}} = \overline{K_{m,h}\left(\frac{1}{r}\frac{\partial u}{\partial \lambda} + r\frac{\partial v/r}{\partial r}\right)}, \quad (6)$$

$$\overline{\tau_{\lambda z}} = \overline{K_{m,v}\left(\frac{1}{r}\frac{\partial w}{\partial \lambda} + \frac{\partial v}{\partial z}\right)}, \quad (7)$$

and $K_{m,h}$ and $K_{m,v}$ are the model output horizontal and vertical momentum diffusivities, respectively.

The azimuthally-averaged radial momentum equation can be written similarly as

$$\frac{\partial \bar{u}}{\partial t} + \underbrace{\bar{u}\frac{\partial \bar{u}}{\partial r}}_{U_{mr}} + \underbrace{\overline{\left(u'\frac{\partial u'}{\partial r} + \frac{v'}{r}\frac{\partial u'}{\partial \lambda}\right)}}_{U_{eh}} = \underbrace{-\bar{w}\frac{\partial \bar{u}}{\partial z}}_{U_{mv}} \underbrace{-\overline{w'\frac{\partial u'}{\partial z}}}_{U_{ev}}$$
$$\underbrace{+\frac{\bar{v}^2}{r} + f\bar{v} - \frac{1}{\bar{\rho}}\frac{\partial \bar{p}}{\partial r}}_{U_{magf}} + \underbrace{\overline{\frac{v'^2}{r} - \frac{1}{\rho}\frac{\partial p'}{\partial r}}}_{U_{eagf}} + \underbrace{\bar{F}_r}_{U_d} \quad (8)$$

Here, $\bar{F}_r$ is the combined mean horizontal and vertical diffusive tendency of radial momentum, given by:

$$\bar{F}_r = \underbrace{\frac{1}{r\bar{\rho}}\frac{\partial r\bar{\rho}\,\overline{\tau_{rr}}}{\partial r} - \frac{\overline{\tau_{\lambda\lambda}}}{r}}_{U_{dh}} + \underbrace{\frac{1}{\bar{\rho}}\frac{\partial \bar{\rho}\,\overline{\tau_{rz}}}{\partial z}}_{U_{dz}}, \quad (9)$$

where the stress tensors (e.g. Landau and Lifshitz, 1966, p51) for the subgrid scale motions[4] are given by

$$\overline{\tau_{rr}} = \overline{2K_{m,h}\left(\frac{\partial u}{\partial r}\right)}, \quad (10)$$

$$\overline{\tau_{\lambda\lambda}} = \overline{2K_{m,h}\left(\frac{1}{r}\frac{\partial v}{\partial \lambda} + \frac{u}{r}\right)}, \quad (11)$$

$$\overline{\tau_{rz}} = \overline{K_{m,v}\left(\frac{\partial u}{\partial z} + \frac{\partial w}{\partial r}\right)}. \quad (12)$$

To facilitate interpretation, we have chosen this pseudo-Lagrangian form in which the left-hand-side represents the material acceleration in the radial direction following the horizontal wind[5]. The pseudo-Lagrangian form is preferred here because it facilitates a layer-wise perspective on the formation of the upper-tropospheric inflow and outflow layers. The individual terms on the left-hand-side represent: the local tendency of the mean radial velocity, the mean radial advection of radial momentum per unit mass, U_{mr}, and the mean horizontal advection of eddy radial momentum, U_{eh} per unit mass. The terms on the right-hand-side of the equation are in order: U_{mv} is minus the mean vertical advection of mean radial momentum per unit mass and U_{ev} is minus the eddy vertical advection of eddy radial momentum per unit mass; U_{magf} and U_{eagf} are the mean and eddy agradient force per unit mass, respectively; and U_d is the combined mean radial and vertical diffusive tendency of radial momentum.

Note that we have chosen to write U_{magf} with $\bar{\rho}$ in the denominator. This choice requires that the azimuthal variation of ρ be retained in the definition of U_{eagf}, and assumes that $|\rho - \bar{\rho}| << \rho$, which is always well satisfied in these numerical experiments.

4.1.1 Attributes of the mean-eddy flow partitioning

The foregoing partitioning of the flow into azimuthal mean and eddy contributions is a natural one for an isolated vortex, especially when applied to vortex waves (e.g. Reasor and Montgomery 2015 and refs.). Nevertheless, care is required when interpreting the individual contributions when strong and highly azimuthally-localized features punctuate the vortex flow in a particular annulus. This is because such localized features project on both components of the partition. For example, an individual updraught within this annulus will project both into the mean and eddy components. However, the mean updraught will have a small positive value while the eddy will have a large positive value in its particular location, but a small negative value elsewhere, a consequence of the partitioning result that $\overline{w'} = 0$. The small negative value for the eddy will identically cancel the small positive value from the mean outside the region of the eddy.

Another issue with this partitioning is that, because the vortex centre is not exactly stationary, there is a weak flow across the vortex axis, even in the problem studied here where the vortex environment is quiescent. Since there is no source or sink of mass at the axis, both $\bar{u}$ and $\bar{v}$ must vanish at the axis, the latter since the vorticity at the axis is finite. As a result, both mean tendency terms must be zero implying that the sums of terms on the right-hand-sides of Equations (4) and (8) must sum to zero at the axis. Because one of the terms in the expressions for U_{eh} and U_{eagf} involve v'/r, and v' may be finite at the axis, these terms must cancel. However, on a finite mesh, this cancellation may be susceptible to appreciable numerical discretization error.

Despite the foregoing cancellation issue, the formulation in terms of mean and eddy components is generally useful for providing insight as long as this attribute of the partitioning is borne in mind. As an example, the effects of eddy momentum fluxes associated with velocity perturbations due to a single updraught on the tangential-mean velocity tendency were investigated by Kilroy and Smith (2016) and a conceptual framework for the interpretation of these eddy fluxes was given.

[4]The expression for $\overline{\tau_{rz}}$ corrects the expression given in Persing *et al.* (2013, their Eq. (20)) and Montgomery and Smith (2017, their Eq. (15)). The difference is found to be negligible.

[5]This choice is different from that for the tangential momentum equation and means that the sum of terms on the right-hand-side can be interpreted as forces that produce pseudo-material acceleration in the radial direction. Such a choice is perhaps less appropriate in the tangential momentum equation as one would then lose the neat form of the radial vorticity flux term.

4.2 Tangential velocity tendency analysis

4.2.1 Spin-up at 36 h

Figure 3 shows radius-height plots of the three-hour time averaged terms in the azimuthally-averaged tangential velocity tendency equation at 36 h, which is during the period of rapid intensification (Figure 1). The time average is based on model output saved every 15 minutes. Panels (a) and (b) show the contributions to the tendency from the mean radial vorticity flux and vertical advection, while panels (c) and (d) show the corresponding eddy contributions. Panels (e) and (f) show the sum of the mean and eddy terms, respectively. In each panel shown the mean eyewall updraught is highlighted by the thick yellow contour, which shows the location of the 0.5 m s^{-1} vertical velocity isopleth, and the pink contours show the ± 1 m s^{-1} radial velocity. So as to provide a spatial reference of the acceleration terms, the green curve shows the azimuthally averaged radius of maximum tangential velocity up to 16 km height.

The mean vorticity influx (panel (a)) is large and positive in a shallow layer near the surface, marking the boundary layer inflow region, and it is large and negative in a narrow sloping sheath just above this layer in the inner core. It is large and negative also in the eyewall updraught, extending into the upper tropospheric outflow layer. There are a few small regions of positive vorticity flux, including a larger more coherent region in the outflow layer outside a radius of about 80 km. The principal features in the mean tendency from vertical advection (panel (b)) are similar to those in panel (a), but are opposite in sign so that there is considerable cancellation as seen in panel (e). This cancellation is a reflection of the fact that above the boundary layer, absolute angular momentum is approximately conserved (see Appendix of Smith *et al.* 2009).

From the perspective of the mean dynamics, the main contribution to the spin-up of the tangential wind is associated with the import of mean cyclonic absolute vorticity in the boundary layer and the vertical advection of tangential momentum so generated into the eyewall updraught. However, there is a region spanning between 1 and 3 km where the *mean* tendencies give a spin down effect (panel (e)). This spin down is more than negated by the vertical eddy momentum transport discussed below.

The contribution to the mean tendency from the eddies are confined mainly to the eyewall updraught region. The eddy vorticity flux term is mostly negative (panel (c)), but there is a region of positive tendency above about 12 km in the outflow region. The vertical advection of eddy tangential momentum (panel (d)) is relatively large and positive below a height of 4 km, but has more of a dipole structure above this level with positive tendencies on the inner part of the eyewall updraught and negative tendencies on the outside. The combined eddy tendency in panel (f) shows a pattern that is quite similar to the sum of the mean tendencies (panel (e)), but of opposite sign[6]. Also, the combined eddy tendency in the eyewall region spanning approximately 1 to 3 km more than compensates the spin down effect from the combined mean terms. In essence, the vertical momentum transport in this layer is taking place principally by the convective eddy structures - affirming the findings of Persing *et al.*

The horizontal diffusive tendency shows a weak negative tendency in the eyewall (panel (g)), while the vertical diffusive tendency is strongly negative in a shallow layer near the surface with a small region of positive tendency below the base of the eyewall updraught. Comparing the radial and vertical eddy terms with the corresponding sub grid-scale diffusion terms shows that the pattern of the eddy terms is generally quite different from that of the diffusion terms. The discrepancy in the pattern of tendencies implies that the resolved eddy contributions cannot be regarded simply as a down-gradient diffusive process. Persing *et al.* (2013) arrived at a similar conclusion in their study.

Comparing panels (a) and (h) one sees that the horizontal vorticity influx is generally larger than the mean vertical diffusion tendency. Even after adding the slight negative tendency from the combined eddy term near the surface, the net tendency of tangential wind (panel (i)) is positive in the inner-core boundary layer. In essence, this is confirmation that the nonlinear boundary layer spin up mechanism[7] is operating to spin up the maximum tangential wind in the boundary layer. Another manifestation of this spin up mechanism is the outward sloping region of positive values below about 4 km in height in panel (d). The positive values of v', which presumably contribute to the supergradient excess, are being lofted to give the values of V_{ev} and must be generated within the boundary layer. These positive tendency values in panel (d) must be a result of the nonlinear boundary layer spin-up mechanism, which acts on the asymmetric component of flow also.

The time-averaged tangential velocity tendency calculated directly from the model output is shown in panel (j). This tendency is simply the difference in tangential velocity over the 3 hour period divided by the 3 hour time span. The panel shows clearly that there is spin up throughout much of the eyewall updraught, including the boundary layer beneath the eyewall and extending to approximately 60 km radius.

This direct tendency can be compared with the estimate from the sum of tendency terms (panel (i)) on the right-hand-side of Equation (4). While the direct calculation is a little smoother, the estimate does show broad agreement with the direct calculation including, in particular, a sloping band of strong positive tendency, mostly inside the 1 m s^{-1} eyewall updraught contour. The most notable discrepancy between these two panels is found in

[6]This tendency for cancellation is perhaps not surprising bearing in mind that the coherent eddy structures have compensating imprints on both the mean and eddy contributions in this simple azimuthal mean and eddy partitioning.

[7]See e.g. Smith and Montgomery (2016).

Tangential wind tendencies at 36 h

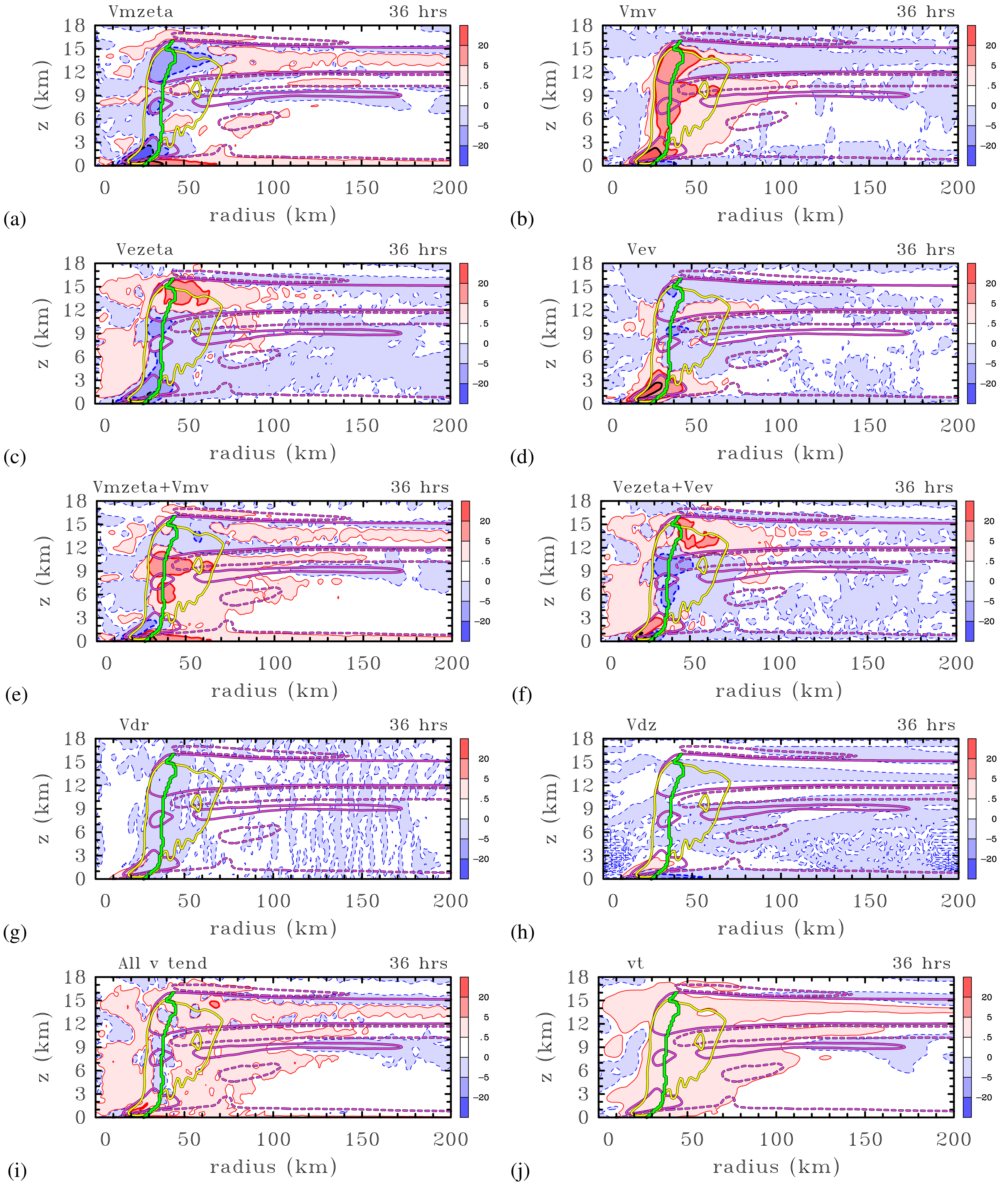

Figure 3. Radius-height plots of the three hour time averaged terms in the azimuthally-averaged tangential wind tendency equation at 36 h. The time averaging is centred on the time shown. Shading as indicated on the side bar in m s^{-1} h^{-1}, with shaded regions enclosed by contours. Thick black contour $\pm$ 20 m s^{-1} h^{-1}. The yellow contour shows the 0.5 m s^{-1} vertical velocity, while the pink contours show $\pm$ 1 m s^{-1} radial velocity. The green curve shows the azimuthally averaged r_{vmax}. Solid contours positive, dashed contours negative.

the eyewall between heights of 3 and 11 km, where there is a small region of negative tendency centred around 35 km radius, straddling the radius of maximum wind at this time. Possible sources for the error in the sum of tendency terms are discussed by Persing *et al.* (2013, p12318). In brief, there are principally three sources of error: the coarse temporal sampling of output data, the evaluation of parameterized internal diffusion and surface momentum fluxes, and the use of centred spatial differences to calculate all advection terms (The CM1 model uses a 5th-order upstream advection scheme). Notwithstanding the relatively small discrepancy within this portion of the eyewall updraught, the broad agreement elsewhere between the two calculations provides strong support to the physical interpretations of the various tendency terms given above.

4.2.2 Later times

Similar radius-height plots to those in Figure 3 have been constructed for 48 h and 72 h (not shown), which are during the period of rapid intensification also (Figure 1). The individual tendency terms have structures that are similar to their counterparts in Figure 3, but are generally larger in magnitude on account of the quadratic nonlinearity of the momentum equations. In particular, there is still a strong mean tendency associated with the radial influx of vorticity in the boundary layer, which is partly opposed by the negative tendency due to friction. Significantly, the strong negative mean tendency $V_{m\zeta} + V_{mv}$ where the air ascends as it exits the boundary layer is opposed by a positive tendency by the sum of the eddy terms $V_{e\zeta} + V_{ev}$. This implies, again, that the eddies are playing an important role in intensifying the swirling flow in the eyewall. In the upper part of the eyewall, there is much cancellation between the sums $V_{m\zeta} + V_{mv}$ and $V_{e\zeta} + V_{ev}$. Another feature that develops at these later time is a region of alternating positive and negative $V_{m\zeta}$ from the surface to a height of 3 km. This feature is a manifestation of the centrifugal recoil effect (see e.g. Montgomery and Smith 2017 and refs.).

4.3 Radial velocity tendency analysis

4.3.1 Spin-up at 36 h

Figure 4 shows radius-height plots of the three-hour time-averaged terms in the azimuthally-averaged, pseudo-Lagrangian radial momentum equation at 36 h. Selected contours of azimuthal and time mean radial velocity are superposed on all panels to facilitate interpretation of the radial momentum dynamics. The radius of maximum azimuthally-averaged tangential velocity is superposed for interpretation purposes also. Panels (a) and (b) show the mean agradient force field, U_{magf} and the mean radial advection (U_{mr}) tendency. As expected, U_{magf} is strongly negative in a shallow surface-based layer at radii beyond about 30 km. This negative region coincides with the frictional boundary layer and *it is primarily this negative force that drives the boundary layer inflow*. Kilroy *et al.* (2016) showed that much of the low-level inflow can be attributed to boundary layer dynamics, whereupon the “suction effect” of deep convection plays a secondary role.

Near the surface, the magnitude of U_{magf} increases with decreasing radius to about 50 km and then declines rapidly. The corresponding tangential winds in this region of negative values are *subgradient*. The mean radial wind progressively increases with decreasing radius in this layer (see, e.g., Fig. 2a), reaching values of about 15 m s^{-1}, which is a significant fraction (about 38%) of the tangential winds in the same region.

Inside approximately 50 km radius and in a shallow layer that slopes upwards with radius, U_{magf} is strongly positive and serves to decelerate the inflow and even accelerate the flow outwards just above the boundary layer into the eyewall updraught. In this positive region, the tangential winds are *supergradient*. There is a negative region between heights of about 2 and 4 km. Above the negative region, U_{magf} is generally positive, being particularly strong in the inner portion of the eyewall updraught and in the outflow region to more than 100 km radius. This pattern is not surprising because air with high angular momentum is being transported vertically by deep convective cores in the developing eyewall.

In the upper troposphere there is a region of positive U_{magf} near the top of the developing eyewall, which is thickest near its top and tapering to zero at a radius of about 120 km. The remainder of the upper troposphere, indeed, in much of the lower troposphere beyond the developing eyewall updraught, has mostly negative values of U_{magf}, with magnitude not more than 5 m s^{-1} h^{-1} The subgradient tangential wind in this region is acting to decelerate outflow and accelerate inflow.

The structure of the mean radial advection U_{mr} shows a shallow layer of negative values beyond a radius of about 35 km *at the surface* where the flow in the boundary layer is accelerating inwards. It shows also shallow sloping layers of alternating positive and negative values, generally confined within a radius of 50 km and a height of about 3 km. The lowermost layer of positive values coincides with the radii where the inflow is decelerated sharply before ascending into the eyewall.

In the upper troposphere, the radial flow accelerates outwards as the air exits the eyewall, but the region of outward acceleration is sandwiched by layers where $U_{mr} < 0$ outside a radius of about 60 km. Beyond approximately 90 km radius, the mean acceleration in the upper troposphere is inwards so that outward flowing air is being decelerated, consistent with the pattern of U_{magf}. Moreover, inspection of the time-mean inflow (purple dash contours) during this same time interval shows that there are regions of inflow sandwiching the outflow layer and these regions overlap with that of negative U_{magf} and U_{mr}. Where this occurs, the flow in the inflow layers will be accelerated inwards.

The radius-height structure of the mean vertical advection U_{mv} in panel (c) shows a series of layers in which U_{mv} has alternating sign. In the lowest layer, near the base of

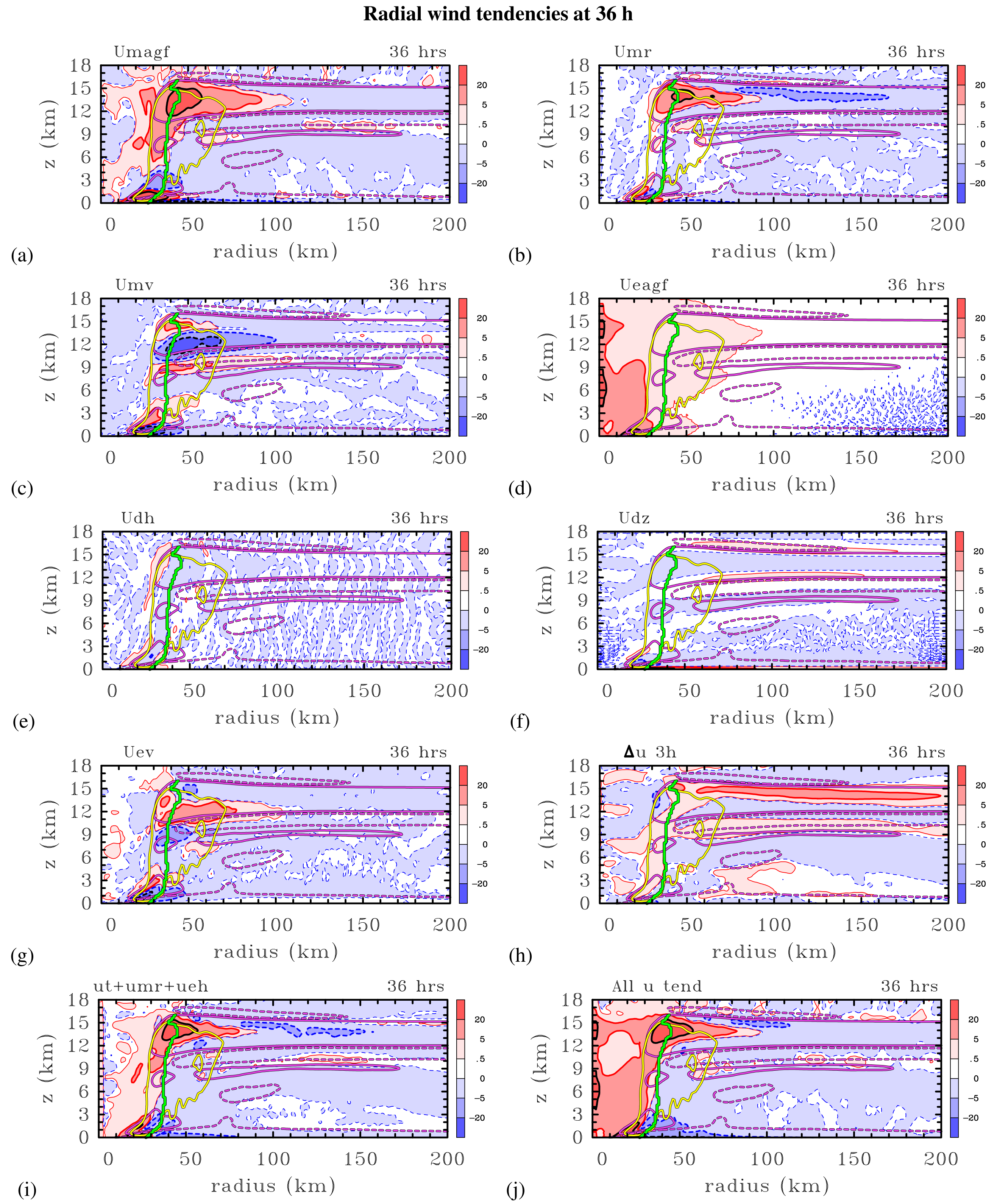

Figure 4. Radius-height plots of the three hour time-averaged terms in the azimuthally-averaged radial wind tendency equation at 36 h. The time averaging is centred on the time shown. Shading as indicated on the side bar in m s^{-1} h^{-1}, with shaded regions enclosed by contours. Thick black contour $\pm$ 20 m s^{-1} h^{-1}. The yellow contour shows the 0.5 m s^{-1} vertical velocity, while the pink contours show $\pm$ 1 m s^{-1} radial velocity. The green curve shows the azimuthally averaged r_{vmax}. Solid contours positive, dashed contours negative.

the developing eyewall updraught, $U_{mv} < 0$, indicating a contribution to an increase of the radial inflow by the vertical advection of inward radial momentum from near the surface. In the sloping layer above, $U_{mv} > 0$, reflecting the mean vertical transport of positive radial momentum associated with the strong outflow of air just above the boundary layer. The layer of negative U_{mv} between about 5 and 8 km height is associated with the upward transport of mean radial inflow in the eyewall updraught from the lower troposphere. The layered pattern of U_{mv} above about 8 km is consistent also with the layered pattern of inflow and outflow in the upper troposphere together with that of vertical velocity. For example, the upward transport of mean inward radial momentum from the inflow layer just below the mean outflow layer together with the downward transport of inward radial momentum from the inflow layer just above the mean outflow layer contribute to the layer of negative tendency centred at an altitude of about 12 km.

The eddy agradient force field, U_{eagf}, in Figure 4d indicates that the asymmetric part of the tangential flow is not in gradient wind balance. This eddy term contributes to a positive radial acceleration throughout the troposphere out to between 50-90 km radius, where it represents an additional centrifuge effect to that of the mean term U_{magf}. In particular, U_{eagf} shows strong positive values near the surface at radii between approximately 10 and 30 km near where the surface inflow terminates, reinforcing the deceleration of the boundary layer inflow. The relatively large values of U_{eagf} near the axis should not be taken too seriously and are presumably due to numerical inaccuracy as discussed in section 4.1.1.

Figures 4e and 4f show the time-averaged and azimuthally-averaged sub-grid-scale tendencies, U_{dh} and U_{dz}. The horizontal diffusion of radial momentum (U_{dh}) is relatively small except in the region where the radial flow terminates and turns up into the eyewall. The vertical diffusion of radial momentum (U_{dz}) shows a very shallow layer of strong positive tendency beyond a radius of about 30 km, which is a manifestation of surface friction slowing down the inflow. Above this layer lies a somewhat thicker layer of negative tendency, which is associated with the vertical diffusion of inward radial momentum through the inflow layer. This diffusion becomes particularly strong near where the boundary layer inflow terminates.

Figure 4g shows minus the eddy vertical advection of eddy vertical momentum per unit mass, U_{ev}. The structure of this term, like U_{mv}, exhibits a series of layers in which U_{ev} has alternating sign. In the lower troposphere, the U_{ev} field broadly reinforces that of U_{mv}. In the upper troposphere there is a degree of cancellation between U_{mv} and U_{ev}, but the eddies can be seen to be reinforcing the strong outflow in the layer between about 11 and 14 km in height. This layer lies below the axis of the upper-level outflow layer, which implies that the eddies are acting to transport radial momentum against the mean gradient in this layer, i.e. they are counter-gradient. In contrast, the layer of negative U_{ev} in the height range 14-16 km lies above the axis of the outflow layer and acts to slow down the outflow in this layer. Further, the layer of negative U_{ev} in the height range 8-11 km overlaps with the pronounced inflow layer just below the outflow layer and acts to reinforce the inflow in this layer. These features are consistent with the upper-level pattern of the vertical eddy momentum flux shown in Persing *et al.* (2013; Figure 15(e)) and contribute to a strengthening of the primary outflow layer, itself, as well as the inflow layer below the outflow layer.

Figure 4h shows the local mean change in radial wind averaged over the three hour period (Δu), which if divided by the time period would give the local tendency $\partial \bar{u}/\partial t$. The figure indicates that over this time interval there has been a strengthening of the overturning circulation. In particular the low-level inflow has strengthened, the outflow just above the boundary layer where the boundary layer terminates has strengthened, and the upper-level outflow has strengthened. In addition, a region of inflow being drawn in by the developing eyewall updraught in a layer between 4 and 8 km in height has strengthened.

4.3.2 Validity of generalized Ekman balance?

In recent years, generalized Ekman balance has been invoked to help explain the dynamics of the tropical cyclone boundary layer during steady-state, spin up and secondary eyewall formation phases (e.g., Kepert 2001, Kepert and Wang 2001, Kepert 2013). Like traditional Ekman balance (e.g., Gill 1982) comprising a balance between pressure gradient, Coriolis and viscous forces in the atmospheric boundary layer, generalized Ekman balance involves a balance between pressure gradient, generalized Coriolis and viscous forces. This vortex Ekman balance, and issues concerning its interpretation for tropical cyclone vortices, are reviewed and analyzed by Smith and Montgomery (2019). In the notation of section 4, the generalized Ekman balance in the radial direction takes the form:

$$0 = U_{magf} + U_{dz} \tag{13}$$

where U_{magf} is the agradient force defined in section 4 (equal to the sum of radial pressure gradient, Coriolis and centrifugal forces), $U_{dz} = K_v \partial^2 \bar{u}/\partial z^2$ is the vertical diffusion of radial momentum and K_v the vertical momentum diffusivity. Although this generalized balance is comprised strictly of the linearized form of U_{magf}, we will, for simplicity, retain the un-approximated form here. As is evident after inspecting Figs. 4(a) and (f), although this balance is reasonably satisfied in the outer vortex boundary layer, it is not at all satisfied in the inner-core boundary layer around the radius of maximum tangential wind wherein U_{dz} is small in comparison to U_{magf}. Indeed, Fig. 4 shows that within approximately 70 km from the vortex center, all terms, save for the radial diffusion, U_{dh}, contribute markedly to the radial momentum balance in the corner flow region of the developing vortex. In particular, the radial advection of mean radial velocity, U_{mr} and the vertical advection of mean radial velocity, U_{mv} make significant contributions to the radial acceleration just outside and underneath the eyewall complex. The eddy centrifugal acceleration U_{eagf} and eddy vertical advection of eddy radial velocity U_{ev} are non-negligible also in this region. These results are found to hold true at later times during the intensification process (not shown), and can be anticipated by the quadratic nonlinearity of the equations as the vortex strengthens.

A similar assessment may be conducted for the vortex Ekman balance in the tangential direction comprising a balance between the mean vorticity influx and the retardation of tangential momentum by vertical diffusion into the underlying ocean, i.e.,

$$0 = V_{m\zeta} + V_{dz} \tag{14}$$

where $V_{m\zeta}$ is the mean vorticity influx as defined in section 4, and $V_{dz} = K_v \partial^2 \bar{v}/\partial z^2$ is the vertical diffusion of tangential momentum. In the simple case of an axisymmetric vortex, there is no pressure gradient force in the azimuthal direction and so this force does not appear in the leading-order balance given by Eq. (14). As in the above assessment of radial Ekman balance, we do not here separate the linear (gradient) and nonlinear (agradient) terms in the vorticity influx term. Inspecting Figs. 3(a) and (h), the tangential Ekman balance is reasonably satisfied in the outer vortex boundary layer beyond approximately 100 km radius. However, it is not well satisfied within approximately 70 km radius, especially around the RMW wherein $V_{m\zeta}$ markedly exceeds V_{dz}. Indeed, Fig. 4 shows that within approximately 70 km from the vortex center, all terms, save for horizontal diffusion (V_{dh}) contribute markedly to the mean tangential velocity tendency. In particular, the vertical advection of mean and eddy tangential velocity, V_{mv} and V_{ev}, respectively, make significant contributions to the mean tendency near the RMW in the boundary layer. Again, these results are found to hold true at later times (not shown). Therefore, as with the radial Ekman balance, tangential Ekman balance is a poor approximation in the high wind region of the vortex and cause and effect arguments using this balance during vortex spin up are suspect and should be avoided.

In summary, the foregoing findings point to the inconsistency of the generalized Ekman balance in the inner-core boundary layer during vortex spin up and extend the findings and related interpretations of Abarca *et al.* (2015).

4.3.3 Summary of radial velocity analysis at 36 h

Although the Δu field clearly indicates the change in the radial flow during the three hour time period, one can explain this change only in terms of the radial force field and the response thereto. The essence of the radial momentum budget is encapsulated in Figures 4i and 4j, which show the sum of the time-averaged and azimuthally-averaged tendencies on each side of Equation (8). Panel (i) shows the time-averaged pseudo-Lagrangian radial acceleration, while panel (j) shows the corresponding net time-averaged net radial force leading to this acceleration. Generally, the principal features of these two fields match each other quite well, despite there being a few local discrepancies in detail that are presumably associated with interpolation errors and the like (see section 4.2.1).

Broadly speaking, there is a net inward force field through much of the lower troposphere including much of the developing eyewall region, itself. This inward force is particularly strong in the inner-core boundary layer. Near the surface and just below the eyewall updraught, this time-averaged force exceeds 5 m s^{-1} h^{-1}. Inside the developing eyewall, near its inner edge, and throughout much of the upper troposphere out to a radius of about 100 km, there is strong positive radial acceleration, exceeding 20 m s^{-1} h^{-1} in the upper troposphere. The net radial force is associated primarily with the pattern of mean agradient force and the mean and eddy vertical advection terms (panels (a), (c) and (g)).

In summary, the flow in much of the inner-core region is significantly unbalanced in the radial direction, especially at low levels and in the upper troposphere. This finding strongly supports the results and interpretations of Zhang *et al.* (2001). Thus, while the assumption of gradient wind balance may be a reasonable zero-order approximation through much of the middle troposphere during spin up, the assumption cannot be justified in the inner-core boundary layer or in the upper troposphere in the region of strong outflow. The radial force fields demonstrate that even a generalized Ekman balance (i.e. a balance between the linearized form of U_{magf} and U_{dz}) is strongly violated in the inner-core boundary layer, where the terms U_{mv}, U_{ev} and U_{eagf} are comparable in magnitude to U_{magf} and cannot be neglected in a zero-order approximation. These results are in line with the findings of Vogl and Smith (2009), Abarca *et al.* (2015) and Smith and Montgomery (2019).

4.3.4 Later times

Similar radius-height cross-sections to those in Figure 4 have been constructed at 48 h and 72 h (not shown). The tendencies in the individual panels have structures that are similar to their counterparts in Figure 4, but, as in the case of the tangential tendency equation, the fields are generally larger in magnitude consistent with the quadratic nonlinearity of the momentum equations. In particular, there is good agreement between the mean pseudo-Lagrangian tendencies shown in panel (i) and the sum of the radial force contributions in panel (j). Moreover, the degree of radial force imbalance increases considerably and the region of imbalance increases in areal extent. These increases are particularly striking in both the lowest 2 km and in the upper troposphere between about 10 and 16 km. Another noteworthy feature is the development of a standing centrifugal wave near the base of the eyewall.

Just above a positive region of U_{magf} is a shallow sloping region. This region, and the two regions of alternating sign below it, represent the primary driving forces for the standing centrifugal wave.

4.3.5 Upper-level inflow jets

The existence of the inward agradient force provides an explanation for the occurrence of inflow layers that sandwich the upper-tropospheric outflow layer. As pointed out by Wang *et al.* (2020), a way to think about the upper-layer outflow layer is to consider it as an expanding jet of air emanating from a radial momentum source where the eyewall convection terminates (Ooyama, 1987). The outward expansion is resisted by an induced radially-inward pressure gradient force (e.g. Smith *et al.* 2018, Fig. 5c,d), recalling that the centrifugal force is always positive and the Coriolis force in the radial direction is positive as long as the tangential flow remains cyclonic. Because the induced pressure field extends beyond just the outflow layer itself, one can expect a flow response laterally beyond the outflow layer as well. Where this inward force persists, it will act to accelerate air parcels inwards.

A more thorough investigation of these inflow jets is presented in a separate study in which the vertical resolution is increased in the upper troposphere at the expense of that in low levels within the frictional boundary layer (Wang *et al.* 2020). In particular, Wang *et al.* show that the inflow jets have a significant degree of azimuthal asymmetry.

5 Conclusions

We have used a high-resolution, three-dimension simulation to explore new aspects of vortex spin up in the framework of the rotating-convection paradigm. As in previous studies, the maximum tangential and radial winds are found to occur within and near the top of the vortex boundary layer. As the mean vortex intensifies, spin up in the boundary layer is accompanied by the development of azimuthal-mean supergradient winds that exceed the gradient wind by up to 20%. Reflecting the strong radial inflow in the boundary layer, the maximum mean tangential wind occurs as much as 10 km inside the maximum gradient wind. The wind asymmetries, associated in part with the asymmetric deep convection, make a substantive contribution ($\sim$30%) to the maximum wind speed inside the radius of this maximum.

As is well known, the boundary layer dynamics cannot be considered strictly in isolation as it depends on the vortex evolution above the boundary layer, which, itself, depends on the ability of the convection to amplify the winds above the boundary layer by the classical spin up mechanism. An improved understanding of the flow within and above the boundary layer is afforded by an analysis of *both* the azimuthal-mean tangential and radial wind tendency equations during vortex spin up. Here we have extended previous work to a higher spatial resolution of 1 km horizontal grid spacing and quantified the net effect of convective eddies and the associated waves they generate on the mean tangential and radial momentum dynamics of the intensifying vortex.

In particular, an analysis of the tangential velocity tendency equation shows that the eddies make a substantial contribution to the spin up of the eyewall region confirming previous findings. An analysis of the force fields in the radial velocity tendency equation highlights a significant degree of gradient wind imbalance in much of the inner-core vortex. This analysis provides also an explanation of forces responsible for the occurrence of inflow layers sandwiching the upper tropospheric outflow layer.

In recent years, a generalized Ekman balance has been advocated to explain vortex boundary layer structure during spin up and secondary eyewall formation. We have shown here that generalized Ekman balance is a poor approximation in the inner-core region during vortex spin up and should not be used to infer cause and effect in the flow structure of the vortex boundary layer.

The results of this study support and extend prior work of Zhang *et al.* (2001) and Persing *et al.* (2013) and point to the significant limitations of a purely axisymmetric and/or balance description of tropical cyclone intensification.

6 Acknowledgements

MTM acknowledges the support of NSF grants AGS-1313948, IAA-1656075, ONR grant N0001417WX00336, and the U. S. Naval Postgraduate School. GK acknowledges financial support for this research from the DFG under grant number KI-2248. The views expressed herein are those of the authors and do not represent sponsoring agencies or institutions.

References

Bryan GH, Fritsch JM. 2002. A benchmark simulation for moist non-hydrostatic numerical models. *Mon. Weather Rev.*, **130**, 2917-2928.

Chen Y, Brunet G, Yau MK. 2003. Spiral bands in a simulated hurricane. Part II: wave activity diagnosis. *J. Atmos. Sci.*, **60**, 12391756.

Črnivec N, Smith RK, Kilroy G. 2016. Dependence of tropical cyclone intensification rate on sea surface temperature. *Q. J. R. Meteor. Soc.*, **142**, 1618-1627.

Dunion JP. 2011. Rewriting the climatology of the tropical North Atlantic and Caribbean Sea atmosphere. *J. Clim.,***24**, 893-908.

Fang J, Zhang F. 2011: Evolution of multiscale vortices in the development of Hurricane Dolly (2008). *J. Atmos. Sci.*, **68** ,103–122.

Gill AE. 1982. Atmosphere-Ocean Dynamics. New York: Academic. 4th ed., 662pp.

Kilroy G, Smith RK, Montgomery MT. 2017: A unified view of tropical cyclogenesis and intensification. *Q. J. R. Meteor. Soc.*, **143**, 450–462.

Kilroy G, Smith RK. 2016. A numerical study of deep convection in tropical cyclones. *Q. J. R. Meteor. Soc.*, **142**, 3138-3151.

Kilroy G, Smith RK, Montgomery MT. 2016. Why do model tropical cyclones grow progressively in size and decay in intensity after reaching maturity? *J. Atmos. Sci.*, **73**, 487-503.

Landau LD, Lifshitz EM. 1966. Fluid Mechanics. Third Revised English Edition. Pergamon Press. 536 pp.

Mapes BE, Zuidema P. 1996: Radiative dynamical consequences of dry tongues in the tropical troposphere. *J. Atmos. Sci.*, **53**, 620–638.

Montgomery MT, Nichols NE, Cram TA, Saunders AB. 2006: A vortical hot tower route to tropical cyclogenesis. *J. Atmos. Sci.*, **63**, 355–386.

Montgomery MT, Smith RK. 2014. Paradigms for tropical cyclone intensification. *Aust. Meteor. Ocean. Journl.*, **64**, 37-66.

Montgomery MT, Smith RK. 2017. Recent developments in the fluid dynamics of tropical cyclones. *Annu. Rev. Fluid Mech.*, **49**, 541-574.

Nguyen VS, Smith RK, Montgomery, MT. 2008: Tropical-cyclone intensification and predictability in three dimensions. *Q. J. R. Meteor. Soc.*, **134**, 563–582.

Ooyama KV. 1987: Numerical experiments of steady and transient jets with a simple model of the hurricane outflow layer. Extended Abstracts, 17th Conf on Hurricanes and Tropical Meteorology, Miami, FI., Amer. Meteor. Soc., 318-320.

Persing J, Montgomery MT, McWilliams J, Smith RK. 2013. Asymmetric and axisymmetric dynamics of tropical cyclones. *Atmos. Chem. Phys.*, **13**, 12249-12341.

Reasor PD, Montgomery MT. 2015. Evaluation of a heuristic model for tropical cyclone resilience. *J. Atmos. Sci.*, **72**, 1765-1782.

Raymond DJ, Kilroy G. 2019: Control of convection in high-resolution simulations of tropical cyclogenesis. *JAMES,* **6**, 1582-1599.

Smith, RK. 2006: Accurate determination of a balanced axisymmetric vortex in a compressible atmosphere. *Tellus*, **58A**, 98-103.

Smith RK, Montgomery MT. 2016. Understanding hurricanes. *Weather*, **71**, 219-223.

Smith RK, Montgomery MT. 2019: The generalized Ekman model for the tropical cyclone boundary layer revisited: the myth of inertial stability as a restoring force. *Q. J. R. Meteor. Soc.*, in review.

Smith RK, Montgomery MT, Vogl S. 2008: A critique of Emanuel's hurricane model and potential intensity theory. *Q. J. R. Meteor. Soc.*, **134**, 551–561.

Smith RK, Montgomery MT, Nguyen SV. 2009. Tropical cyclone spin-up revisited. *Q. J. R. Meteor. Soc.*, **135**, 1321-1335.

Smith RK, Montgomery MT, Kilroy, G. 2018: The generation of kinetic energy in tropical cyclones revisited. *Q. J. R. Meteor. Soc.*, **145**, 2481-2490.

Vogl S, Smith RK. 2009: Limitations of a linear model for the hurricane boundary layer. *Q. J. R. Meteor. Soc.*, **135**, 83917850.

Wang S, Smith RK, Montgomery MT. 2020: Upper tropospheric inflow layers in tropical cyclones. *Q. J. R. Meteor. Soc.*, (submitted Jan 2020).

Zhang JA, Montgomery MT. 2012: Observational estimates of the horizontal eddy diffusivity and mixing length in the low-level region of intense hurricanes, *J. Atmos. Sci.*, **69**, 1306-1316.

Zhang JA, Rogers RF, Nolan DS, Marks Jr. FD. 2011: On the characteristic height scales of the hurricane boundary layer. *Mon. Weather Rev.*, **139**, 2523-2535.